Controlling fracture cascades through twisting and quenching

Ronald H. Heisser[a,b,1], Vishal P. Patil[c,1], Norbert Stoop[c], Emmanuel Villermaux[d,e], and Jörn Dunkel[c,2]

[a]Sibley School of Mechanical and Aerospace Engineering, Cornell University, Ithaca, NY 14853; [b]Department of Mechanical Engineering, Massachusetts Institute of Technology, Cambridge, MA 02139; [c]Department of Mathematics, Massachusetts Institute of Technology, Cambridge, MA 02139; [d]Université Aix Marseille, CNRS, Institut de Recherche sur les Phénomènes Hors Équilibre, F-13384 Marseille, France; and [e]CNRS/MIT/AMU Joint Laboratory MultiScale Materials Science for Energy and Environment, MIT Energy Initiative, Massachusetts Institute of Technology, Cambridge, MA 02139

Edited by Alain Karma, Northeastern University, Boston, MA, and accepted by Editorial Board Member Herbert Levine July 22, 2018 (received for review February 15, 2018)

Fracture fundamentally limits the structural stability of macroscopic and microscopic matter, from beams and bones to microtubules and nanotubes. Despite substantial recent experimental and theoretical progress, fracture control continues to present profound practical and theoretical challenges. While bending-induced fracture of elongated rod-like objects has been intensely studied, the effects of twist and quench dynamics have yet to be explored systematically. Here, we show how twist and quench protocols may be used to control such fracture processes, by revisiting Feynman's observation that dry spaghetti typically breaks into three or more pieces when exposed to large pure bending stresses. Combining theory and experiment, we demonstrate controlled binary fracture of brittle elastic rods for two distinct protocols based on twisting and nonadiabatic quenching. Our experimental data for twist-controlled fracture agree quantitatively with a theoretically predicted phase diagram, and we establish asymptotic scaling relations for quenched fracture. Due to their general character, these results are expected to apply to torsional and kinetic fracture processes in a wide range of systems.

fracture cascade | elastic rods | scaling laws

Elastic rods (ERs) are ubiquitous in natural and man-made matter, performing important physical and biological functions across a wide range of scales, from columns (1), trees (2–4), and bones (5) to the legs of water striders (6), semiflexible polymer (7) networks (8, 9), and carbon nanotube composites (10). When placed under extreme stresses, the structural stability of such materials becomes ultimately limited by the fracture behaviors of their individual fibrous or tubular constituents. Owing to their central practical importance in engineering, ER fracture and crack propagation have been intensively studied for more than a century both experimentally (11–13) and theoretically (14–16). Recent advances in video microscopy and microscale force manipulation (17, 18) have extended the scope of fracture studies to the microworld (19, 20), revealing causes and effects of structural failure in the axonal cytoskeleton (21), fibroblasts (22), bacterial flagellar motors (23), active liquid crystals (8), and multiwalled carbon nanotubes (24, 25).

Built on Sir Neville Mott's foundational studies on the fragmentation of ring-shaped explosives (26), theoretical work on ER fracture has flourished over the past two decades (12, 13, 27–30). However, many basic aspects of the ER fracture phenomenology remain poorly understood. Bending-induced ER fragmentation has been thoroughly investigated in the limits of adiabatically slow (12) and diabatically fast (13) energy injection, but the roles of twist and quench rate on the fracture process have yet to be clarified. These two fundamental issues are directly linked to a famous observation by Richard Feynman (31), who noted that dry spaghetti, when brought to fracture by holding the ends and moving them toward each other, appears almost always to break into at least three pieces. The phenomenon of nonbinary ER fracture is also well known to pole vaulters, with a notable instance occurring during the 2012 Olympic Games (32). Below, we revisit and generalize Feynman's experiment to investigate systematically how twist and quench dynamics influence the elastic fragmentation cascade (12, 13). Specifically, we demonstrate two complementary quench protocols for controlled binary fracture of brittle ERs. Our experimental observations are in agreement with numerical predictions from a nonlinear elasticity model and can be rationalized through analytical scaling arguments.

Results and Discussion

Timescales in Fragmentation. Revisiting Feynman's experiment, we monitor the fracture dynamics of dry spaghetti, using high-speed imaging at frame rates ranging from 1,972 frames per second (fps) to 1,000,000 fps (Fig. 1 and *Materials and Methods*). The highest time-resolution data show that already a basic fracture event involves several timescales, from initial crack nucleation and growth to catastrophic failure (Fig. 1*A* and Movie S1). The initial nucleation phase is relatively slow, lasting $\sim$10 ms. It is followed by a fast catastrophic phase ($\sim$10 μs), during which the crack propagates rapidly close to the material speed of sound. The creation of multiple fragments via a fragmentation

Significance

Fracture processes are ubiquitous in nature, from earthquakes to broken trees and bones. Understanding and controlling fracture dynamics remain one of the foremost theoretical and practical challenges in material science and physics. A well-known problem with direct implications for the fracture behavior of elongated brittle objects, such as vaulting poles or long fibers, goes back to the famous physicist Richard Feynman who observed that dry spaghetti almost always breaks into three or more pieces when exposed to large bending stresses. While bending-induced fracture is fairly well understood nowadays, much less is known about the effects of twist. Our experimental and theoretical results demonstrate that twisting enables remarkable fracture control by using the different propagation speeds of twist and bending waves.

Author contributions: R.H.H., V.P.P., and J.D. designed research; R.H.H., V.P.P., N.S., E.V., and J.D. performed research; R.H.H. and V.P.P. analyzed data; and R.H.H., V.P.P., N.S., E.V., and J.D. wrote the paper.

The authors declare no conflict of interest.

This article is a PNAS Direct Submission. A.K. is a guest editor invited by the Editorial Board.

Data deposition: The Matlab code can be downloaded from https://github.com/vppatil28/elastic_rod_fracture_simulation.

[1]R.H.H. and V.P.P. contributed equally to this work.

[2]To whom correspondence should be addressed. Email: dunkel@mit.edu.

This article contains supporting information online at www.pnas.org/lookup/suppl/doi:10.1073/pnas.1802831115/-/DCSupplemental.

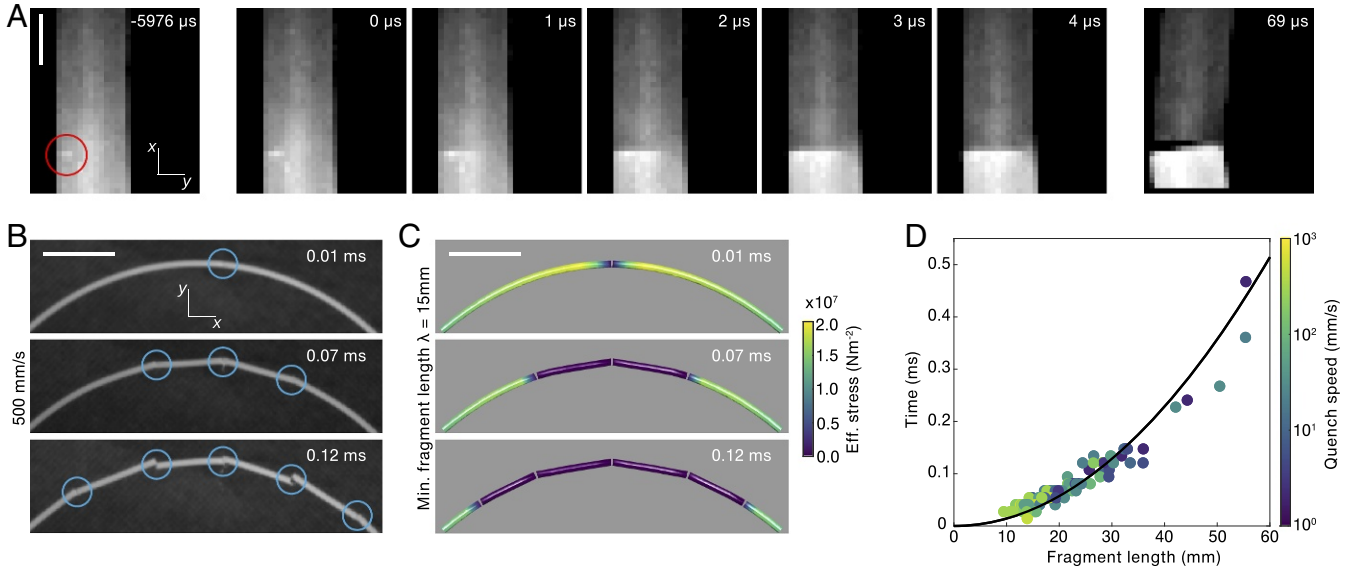

Fig. 1. Fragmentation is a multistage process. (*A*) High-speed images show first fracture (Movie S1). A crack nucleates and grows initially on a relatively slow millisecond timescale. Catastrophic failure occurs at a critical crack depth (the Griffith length) leading to rapid crack propagation within ∼10 μs. Subsequent separation of the two fragments is governed by another slower timescale associated with bending waves. (*B*) High-speed images show sequential fractures separated by a characteristic distance. Fragments are ejected with considerable angular velocity, in agreement with the observation of nonsimultaneous fractures. (*C*) Simulations show bending waves originating at the point of first fracture creating additional fractures separated by at least the minimum fragment length λ. The predicted fracture times agree with *B*. In simulations, fragments are frozen after fracture and do not evolve further. (*D*) The time between the first two fractures and the resulting fragment length lie along the space–time path of the location of maximum bending stress (solid line) (sample size $n = 110$). The distance between the first two fractures depends on quench speed but is bounded from below. Diameter of rod and gaps between fragments are enhanced for visualization in *C*. [Scale bars: (*A*) 1 mm and (*B* and *C*) 15 mm.]

cascade is then governed by the slower propagation timescale of elastic bending waves (Fig. 1 *B* and *C*), as shown by Audoly and Neukirch (12). Our goal is to control the fragmentation dynamics on this slower elastic timescale, which can be treated accurately within the Kirchhoff theory (Fig. 1 *B* and *C*).

Damped Kirchhoff Model. We describe an ER at time t by its arc-length–parametrized centerline $\mathbf{x}(s,t)$, $s \in [0, L]$, and an orthonormal frame $\{\mathbf{d_1}(s,t), \mathbf{d_2}(s,t), \mathbf{d_3}(s,t)\}$ such that $\mathbf{d_3} = \mathbf{x}'$, where primes denote s derivatives and dots denote t derivatives. We further assume the rod is uniform with density ρ, naturally straight and inextensible with circular cross-sectional area $A = \pi r^2$. Its moment of inertia I and moment of twist J are then given by $J = 2I = \pi r^4/2$ (33). The rod's dynamics are governed by the damped Kirchhoff equations (33, 34) (*SI Appendix*, *Kirchhoff Model*)

$$\mathbf{F}'' = \rho A \ddot{\mathbf{d}}_3 \qquad \textbf{[1a]}$$

$$\mathbf{M}' + \mathbf{d_3} \times \mathbf{F} = \dot{\mathbf{L}} + 4b\rho I \omega_3 \mathbf{d_3}, \qquad \textbf{[1b]}$$

where $\mathbf{F}(s,t)$ is the force, $\mathbf{M}(s,t) = EI\kappa_1\mathbf{d_1} + EI\kappa_2\mathbf{d_2} + \mu J\kappa_3\mathbf{d_3}$ is the internal moment, $\mathbf{L}(s,t) = \rho I\omega_1\mathbf{d_1} + \rho I\omega_2\mathbf{d_2} + 2\rho I\omega_3\mathbf{d_3}$ is the cross-sectional angular momentum, and the vectors $\boldsymbol{\kappa} = \kappa_i\mathbf{d_i}$, $\boldsymbol{\omega} = \omega_i\mathbf{d_i}$ satisfy $\mathbf{d_i}' = \boldsymbol{\kappa} \times \mathbf{d_i}$, $\dot{\mathbf{d}}_\mathbf{i} = \boldsymbol{\omega} \times \mathbf{d_i}$. The Young's modulus E and the shear modulus μ are related by $E/\mu = 2(1+\nu)$, where ν is Poisson's ratio. Most materials have $0.2 < \nu < 0.5$. The final term on the right-hand side of Eq. **1b** denotes damping of twist modes with damping parameter b. Our measurements of this parameter using a torsion pendulum indicate that twist is approximately critically damped (*SI Appendix*, *Dissipation of Twist*). Since the timescale for the entire fracture cascade is an order of magnitude smaller than the time period of the fundamental bending mode, we do not need to include bending damping terms in our analysis. The average material properties of our experimental samples are $2r = 1.4 \pm 0.05$ mm, $\rho = 1.5 \pm 0.1\,\mathrm{g/cm^3}$, $E = 3.8 \pm 0.3$ GPa, and $\mu = 1.5 \pm 0.2$ GPa, and by considering mean values for E, μ we obtain $\nu = 0.3 \pm 0.1$ (*SI Appendix*, *Sample Characterization*). We present additional data for rods of radius $2r = 1.7 \pm 0.05$ mm in *SI Appendix*, Fig. S2. Finally, we note that the Kirchhoff equations do not account for certain shear effects described by Timoshenko beam theory. Indeed, the Timoshenko theory does provide a more accurate description of bending waves with large wavenumber compared with rod radius. However, to describe fracture, we will need only to consider wavenumbers k with $kr/2\pi < 0.1$. In this regime, the difference between the Timoshenko and Kirchhoff beam theories is negligible (35).

Minimum Fragment Length. As shown by Audoly and Neukirch (12), when an initially uniformly curved ER is released from one end, its local curvature increases at the free end. However, when a rod fractures at a point of maximum curvature, the Kirchhoff model possesses solutions in which the curvature near the fracture tip increases even further. Assuming a curvature-based fracture criterion, this would trigger additional fractures arbitrarily close to the first fracture, which is not observed experimentally (Fig. 1 *B* and *D*). In agreement with standard fragmentation theory (36, 37), our data show the existence of a finite minimum fragment length $\lambda > 0$ (Fig. 1*D*). This observation, along with the separation of bending wave and crack propagation timescales (Fig. 1*A*), confirms the applicability of the Kirchhoff theory (Fig. 1 *B* and *C*).

Fracture Criteria. To compare individual experiments with theoretical predictions, we solve the Kirchhoff Eqs. **1a** and **1b** numerically with a discrete differential geometry algorithm (38, 39) (*Materials and Methods*), adopting a stress-based fracture criterion defined as follows: We define the twist of the rod, $\theta(s,t)$, from the twist density, $\kappa_3(s,t)$, by $\theta' = \kappa_3$. The effective stress at a point, $\sigma(s)$, is obtained by integrating a scalar invariant of the full stress tensor, $\hat{\boldsymbol{S}}$, over a cross-section of the rod,

$$\sigma(s,t)^2 = \frac{1}{2\pi r^2}\int \mathrm{tr}\left(\hat{\boldsymbol{S}}^\top \hat{\boldsymbol{S}}\right) dA = \frac{1}{4}E^2 r^2 \kappa(s,t)^2 + \frac{1}{2}\mu^2 r^2 \theta'(s,t)^2, \quad [2]$$

where $\kappa = \left(\kappa_1^2 + \kappa_2^2\right)^{1/2}$ is the centerline curvature of the rod and tr the trace. If the rod is in a steady state, the twist density is constant, $\theta' = Tw/L$, where Tw is the total applied twist.

We posit that the rod fractures at the point s if $\sigma(s)$ exceeds a critical value σ_c that depends on the radius r and material parameters of the rod. We further assume that no two fractures can occur within a minimal fragment length λ of each other. To describe the near-adiabatic twist experiments, we adopt the mean value $\lambda_0 \approx 30$ mm measured at speed ~ 3 mm/s and zero twist (Fig. 1*D*). For a uniform twist distribution, the critical stress imposes a critical yield curvature κ_c. This allows us to introduce a dimensionless parameter describing the relative importance of twist and bending effects in fracture:

$$\mathrm{Li} = \frac{\mu\, Tw}{E\kappa_c L}. \quad [3]$$

We can now rewrite the above expression Eq. **2** for σ_c as

$$\sigma_c^2 = E^2 r^2 \kappa_c^2 \left(\frac{1}{4} + \frac{1}{2}\mathrm{Li}^2\right). \quad [4]$$

For comparison, by integrating the classical von Mises stress criterion over a cross-section, we obtain a critical local stress ellipse given by

$$\left(\sigma_c^{\mathrm{VM}}\right)^2 = E^2 r^2 \kappa_c^2 \left(\frac{1}{4} + \frac{3}{4}\mathrm{Li}^2\right). \quad [5]$$

Another common criterion comes from considering the maximum eigenvalue of the stress tensor, or maximum principal stress, on the boundary of the rod; this gives

$$\left(\sigma_c^{P}\right)^2 = E^2 r^2 \kappa_c^2 \left(1 + \mathrm{Li}^2 + \sqrt{1 + 2\,\mathrm{Li}^2}\right). \quad [6]$$

All three curves are qualitatively consistent with our data, with Eq. **4** yielding the best quantitative agreement (Fig. 2*F*). For samples of different length and radius, and hence a different value σ_c, Eq. **4** is still found to agree well with the data (*SI Appendix*, *Robustness Under Parameter Variations*). In the limit of zero twist, all three fracture criteria predict a critical curvature, which has been successfully used to rationalize aspects of twist-free ER fracture (12). While the origin of this critical curvature requires a deeper theory (30), the above fracture criterion Eq. **4** suffices for our purposes.

Twist-Controlled Fracture. The first protocol explores the role of twist in bending-induced ER fracture. Twisting modes are known to cause many counterintuitive phenomena in ER morphology (40–43), including Michell's instability (44) and supercoiling (45). The motivation for combining twisting and bending to achieve controlled binary fracture is based on the idea that torsional modes can contribute to the first stress-induced fracture but may dissipate sufficiently fast to prevent subsequent

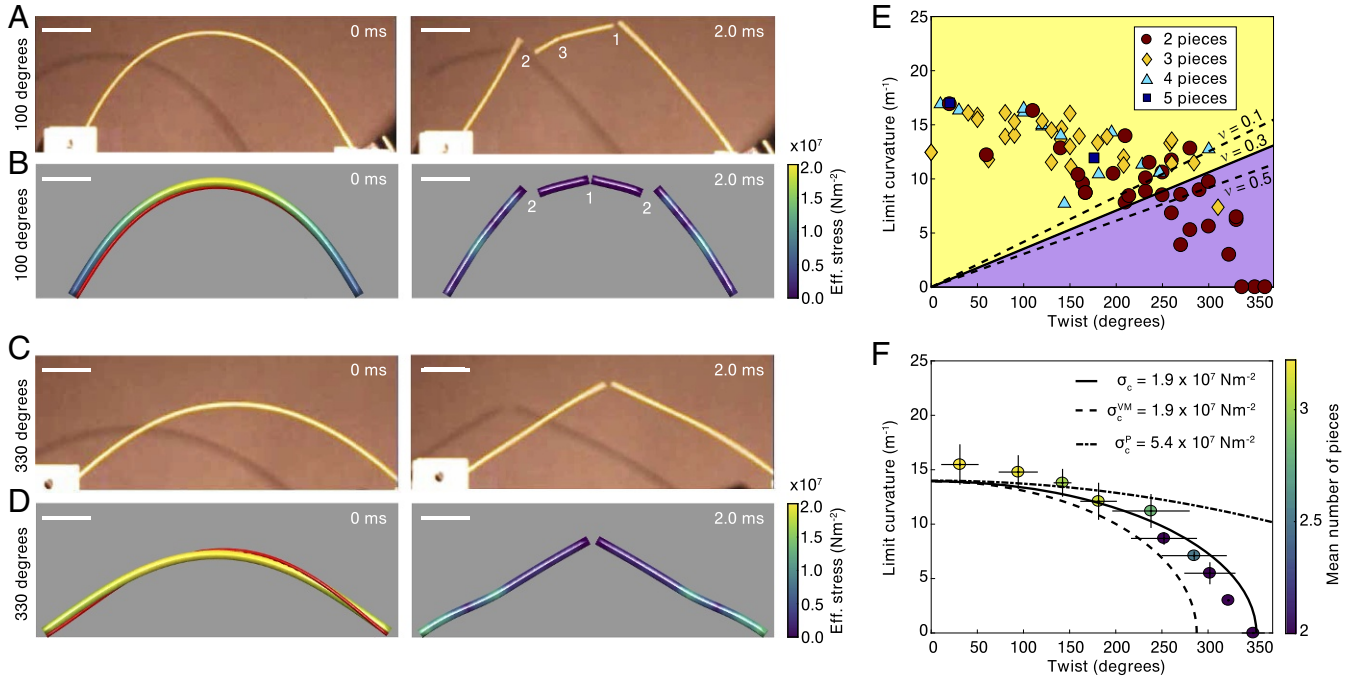

Fig. 2. Using twist to break Feynman's fragmentation bound. (*A*) High-speed images from an experiment with subcritical twist angle showing fragmentation into more than two pieces, in agreement with Feynman's conjecture (Movie S2). Time $t = 0$ (*A*, *Left*) is defined as the moment (last frame) before fracture. (*B*) Simulations also predict fracture in more than two pieces for parameters corresponding to the experiment in *A*. Due to perfectly symmetric initial conditions, our simulations generally produce even fragment numbers (Movie S2). Red line illustrates twist. (*C*) At supercritical twist angles, the maximum curvature before fracture is significantly lowered, enabling twist-controlled binary fracture (Movie S3). (*D*) Simulations for the experimental parameters in *C* also confirm binary fracture (Movie S3). (*E*) Phase diagram showing that binary fracture dominates for twist angles larger than $\sim 250^\circ$ ($n = 73$). The theoretically predicted region (purple) in which an ideal rod is expected to exhibit binary fracture depends only weakly on Poisson's ratio ν and agrees well with the data. (*F*) Experimental data from *E*, averaged over 10 sectors defined by the rays $(\mu^2 JL^{-1}\cos(j\pi/20), E^2 I \sin(j\pi/20))$ for $j = 0, 1 \ldots, 10$, follow the theoretically predicted critical ellipse (solid curve) from Eq. **4**. The dashed curve shows the von Mises ellipse from Eq. **5**, and the dashed-dotted curve shows the parabola of constant maximum principal stress from Eq. **6**. The data in Fig. 3 yield $\sigma_c = \sigma_c^{\mathrm{VM}} = \sigma_c^P/\sqrt{8} = 1.9 \times 10^7$ N/m^2 at zero twist. Error bars show SDs. The critical curvatures for simulations at different twist in *B* and *D* are chosen according to the critical stress ellipse in *F* and the minimum fragment length $\lambda = 30$ mm estimated from the data in Fig. 1*D*. Diameter of the rod in *B* and *D* is enhanced for visualization. [Scale bars (*A*–*D*): 30 mm.]

fractures. To test this hypothesis, we built a custom device consisting of a linear stage with two freely pivoting manual rotary stages placed on both sides (*SI Appendix*, Fig. S1). Aluminum gripping elements were attached to each rotary stage to constrain samples close to the torsional and bending axes of rotation (*SI Appendix*, *Twist Tests*). As in Feynman's original experiment (31), we used commercially available spaghetti as test rods. To ensure reproducibility, individual rods were cut to the same fixed length $L = 24$ cm, and experiments were performed in a narrow temperature and humidity range (*SI Appendix*, *Preparation of Experimental Samples*). The rods' ends were coated with epoxy to increase the frictional contact with the gripping elements, enabling us to twist samples to the point of purely torsional failure, which occurred at $\sim 360^\circ$ for our ERs. In each individual twist experiment, a rod was loaded into the device, twisted to a predetermined angle, and then bent near adiabatically (end-to-end speed <3 mm/s) until fracture occurred. Select trials were recorded with a high-speed camera at 1,972 fps (*SI Appendix*, *Twist Tests*).

As the first main result, our experiments demonstrate that supercritical twist angles give rise to binary fracture (Fig. 2). By contrast, for small twist angles, rods are found to fragment typically into three or more pieces (Fig. 2*A*), in agreement with Feynman's conjecture and supporting recent experimental and theoretical results (12) for the zero-twist case. For large twist angles, however, the maximum curvature before the first fracture is substantially lowered and binary fracture becomes favored (Fig. 2*C*). Although sample inhomogeneities lead to a distribution of fragment numbers at the same twist angles, the average number of fragments exhibits a robust trend toward binary fracture for twist angles larger than $\sim 250^\circ$ (Fig. 2 *E* and *F*). In particular, the experimental data follow a von Mises-type ellipsoidal curve when plotted in the plane spanned by the limit curvature and twist angle (Fig. 2 *E* and *F*). We next rationalize these observations by performing mode analysis using the nonlinear elasticity model.

We consider the dynamics after the first fracture, starting from the fact that twist enables the rod to store its energy in more than one mode. We assume the first fracture occurs at $t = 0$ at the midpoint of the rod, when the curvature exceeds the critical value κ_c determined by Eq. **4**. Our experiments and simulations show that at large twists, the rod breaks with low curvature (Fig. 2 *C*–*F*). Focusing on this limit, we may assume that the rod is approximately planar and that the bending is small. Under these assumptions, the twist density and bending modes uncouple (*SI Appendix*, *Small Deflections*), and the dynamical equation for θ reduces to a damped-wave equation $(\mu/\rho)\theta_{ss} = \theta_{tt} + 2b\theta_t$ for $s \in [0, L/2]$. Similarly, the small-bending assumption allows us to describe the bending dynamics via the Euler–Bernoulli beam equation, $EIy_{ssss} + \rho A y_{tt} = 0$, where the centerline is now given by $y(s, t)$. Scaling arguments simplify the analysis of these equations. The speed of the twist waves is determined by shear modulus and density, $c_\theta = \sqrt{\mu/\rho}$. Enforcing the free-end boundary condition, $\theta'(L/2) = 0$, for the undamped twist equation yields a solution with a region of zero twist stress ($\theta' = 0$) growing at speed c_θ from the $s = L/2$ endpoint (*SI Appendix*, *Dissipation of Twist*). With nonzero damping, this picture is valid for propagation over small distances. In particular, the time taken for the zero twist stress front to travel distance λ_0, the minimum fragment length, is $T_\theta^0 = \lambda_0/c_\theta$. Over longer lengthscales $\ell > \lambda_0$, the damping term becomes important. The zero twist front travels distance ℓ in time $T_\theta^\ell = b\ell^2/c_\theta^2$. Since twist modes are approximately critically damped (*SI Appendix*, *Dissipation of Twist*), with $b \approx \pi c_\theta/L$, we find $T_\theta^\ell = \pi\ell^2/c_\theta L$, implying that twist modes dissipate after a time $T_\theta^{\text{diss}} = L/c_\theta$. We analyze the speed of bending modes in a similar way. Our data show that fractures are caused by the pulse of maximum bending stress (solid line in Fig. 1*D*). Let T_b^0, T_b^ℓ be the time taken for the maximum bending stress to travel distance λ_0, ℓ, respectively. To leading order, it can be shown (12) that $T_b^0/\lambda_0^2 = T_b^\ell/\ell^2 = (1/2\pi r)\sqrt{\rho/E}$ (*SI Appendix*, *Euler–Bernoulli Equation*). This may be understood by observing that the speed of a bending wavepacket peaked at wavenumber k is given by $c_b = 2k\sqrt{EI/\rho A}$. If we take $k = 2\pi/\ell$, then the time taken for the bending wavepacket to travel distance ℓ is $T_b^\ell \approx \ell\left[(4\pi/\ell)\sqrt{EI/\rho A}\right]^{-1} = (\ell^2/2\pi r)\sqrt{\rho/E}$. We can use these results to compare the twist and bending timescales:

$$T_b^0 = \frac{\lambda_0}{2\pi r}\left[\frac{1}{2(1+\nu)}\right]^{\frac{1}{2}} T_\theta^0, \qquad T_b^\ell = \frac{L}{2\pi^2 r}\left[\frac{1}{2(1+\nu)}\right]^{\frac{1}{2}} T_\theta^\ell.$$

Using the measured value $\lambda_0 \approx 30$ mm, we find $T_b^0 > 4T_\theta^0$ and $T_b^\ell > 5T_\theta^\ell$, indicating that twist dissipates before bending waves can trigger another fracture. In addition, we find that $T_\theta^{\text{diss}} \approx 2T_b^0$, which further suggests that twist plays no role in future fracture events. The above difference in propagation times is a robust result. For example, Timoshenko theory predicts even slower bending waves than Euler–Bernoulli theory (35), although both beam models agree very closely in our parameter regime. To complete the argument, we observe that all of the fractures occur before reflection of the bending waves at $s = 0$ becomes important. Another fracture will then be triggered if and only if $\sigma(s, t) > \sigma_c$ for any s satisfying the minimum fragment length criterion and $t \in [0, t_0]$, where t_0 is the time for the high-energy bending waves to reach $s = 0$. Since twist dissipates before the bending waves become relevant, we have $\max_{t\in[0,t_0]} \sigma^2 = E^2 I \max_{t\in[0,t_0]} \kappa^2$. Let C be such that $\max_{t\in[0,t_0]} \kappa = C\kappa_c$. We note that even though twist dissipates quickly, the initial twist still determines the shape of the rod at $t = 0$, so C is a function of $\kappa_c L$, Tw and possibly other parameters. We calculate C numerically from the Kirchhoff equations for our experimental parameters and find to one decimal place $C = 1.5$ for all relevant values of $\kappa_c L$ and Tw (*SI Appendix*, *Euler–Bernoulli Equation*). The criterion that the rod breaks into only two pieces then takes the form $E^2 I C^2 \kappa_c^2 < \sigma_c^2$. Using Eq. **4** to eliminate σ_c, the criterion for binary fracture becomes

$$\kappa_c < \frac{Tw}{\sqrt{2}L(1+\nu)\sqrt{C^2 - 1}}. \qquad [7]$$

In terms of the dimensionless Li number from Eq. **3**, this condition is approximately $\text{Li} > 1$. The right-hand side of this inequality describes a weakly ν-dependent straight line in the curvature-twist plane (Fig. 2*E*). Ideal ERs that undergo their first fracture at values κ_c and Tw satisfying Eq. **7** lie below this line (purple region in Fig. 2*E*) and are expected to break into exactly two pieces. This prediction agrees well with the mean number of fragments measured in our experiments (Fig. 2*F*). Additional data for samples of a different length and radius also show good agreement with Eq. **7** (*SI Appendix*, Fig. S2). The raw data show that binary fracture events can occur with low probability outside the critical region (Fig. 2*E*), which could be caused by sample defects and inhomogeneities. The distinct transition from binary to nonbinary fracture in the averaged data (Fig. 2*F*) indicates, however, that defects do not dominate the fracture statistics. Our results for the low-twist regime are consistent with those of Audoly and Neukirch (12) who reported nonbinary fracture at zero twist. By contrast, binary fracture becomes almost certain in the high-twist regime.

Quench-Controlled Fracture. Twist fracture experiments are carried out for a fixed speed $v = 3$ mm/s in the near-adiabatic regime. To systematically explore how quenching affects ER

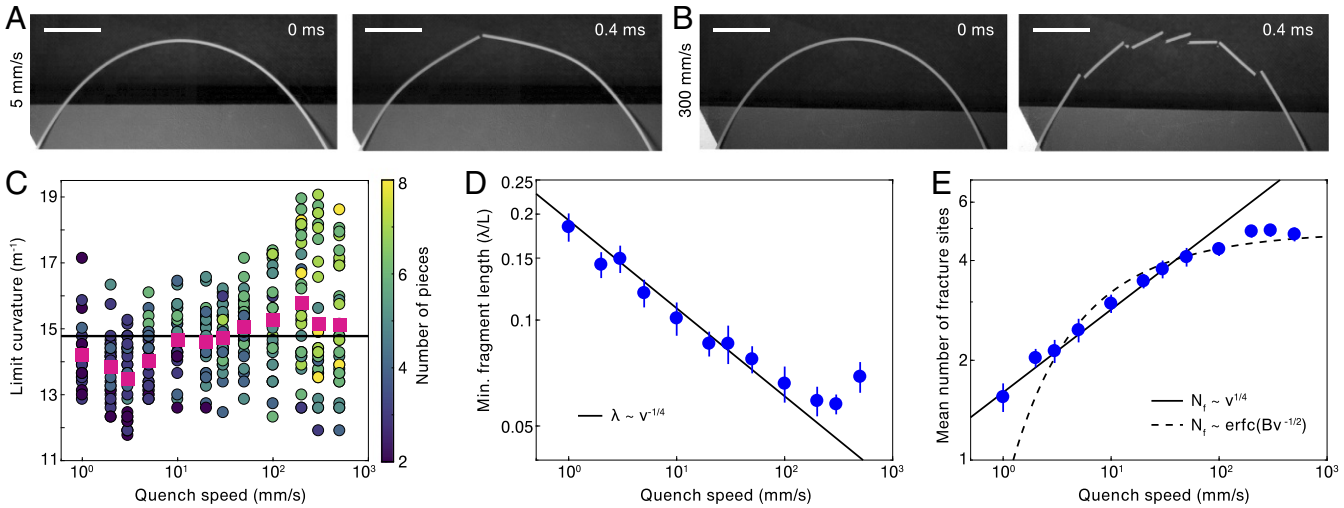

Fig. 3. Dynamically quenched fracture in brittle ERs. (*A*) Experiment at low quench speed v showing binary fracture (Movie S4). (*B*) Experiment at high quench speed v showing fracture into multiple fragments (Movie S5), even though the limit curvature before the first fracture is similar to that in *A*. (*C*) Distributions of the limit curvature (mean values highlighted in pink) are not significantly affected by the quench speed v, but the mean number of fragments increases with v ($n = 350$). (*D*) The mean length of the smallest fragments follows the theoretically predicted power-law scaling. (*E*) At low speed, the number of fracture sites approaches an asymptotic power law (solid line) as expected from *D*. At high speeds, saturation occurs in agreement with stochastic fracture theory (dashed line) (*SI Appendix*). At the lowest quench speed ($v = 1$ mm/s) the rod breaks into fewer than three pieces on average. (Scale bars in A and B, 30 mm.) Error bars in *D* and *E* show SE.

fracture, we built a second fracture device coupling a dc stepper motor to a linear stage (*SI Appendix*, Fig. S1). By adjusting the motor velocity, we can vary v, defined as absolute relative velocity of the ends, by more than two orders of magnitude (Fig. 3). Our nonadiabatic quench protocol allows the rod to bend before fracturing, in contrast to ultrafast diabatic protocols (13) that cause fracture by exciting buckling modes in the unbent state. Previous studies have shown that the fractal nature of fragmentation (46) and disorder (47) can give rise to universal power laws. Here, we will see that nonadiabatic quenching leads to asymptotic power-law relations that involve the quench parameter v.

To investigate how quenched bending dynamics affect fracture, we performed 350 fracture experiments distributed over 12 different quench speeds v ranging from 1 mm/s to 500 mm/s, with rods of length $L = 24$ cm, as in the twist experiments. Experiments were conducted in two batches at different environmental conditions, yielding consistent data (*SI Appendix*, Fig. S2). Select trials were recorded at 75,000 fps (Fig. 3 *A* and *B*). Generally, our experiments show that an increase in the quench speed v has only a weak effect on the curvature before fracture (Fig. 3*C*), in stark contrast to the effects of twist discussed above. Changing v does, however, affect strongly both the minimal size of the fragments (Fig. 3*D*) and the number of fragments (Fig. 3 *E* and *F*). To understand why quench speed (at zero twist) only weakly affects the limit curvature, note that the critical curvature of the samples at first fracture is of the order of $10\,\mathrm{m}^{-1}$ across all experiments (Fig. 3*C*). This means that the potential energy density at the first fracture is $E_P \approx EI\kappa^2 \approx 10^{-1}$ J/m. For comparison, for a hypothetical quench speed of $v = 1$ m/s, considerably higher than realized in our experiments, the kinetic energy density is $E_K \approx \rho A v^2/2 \approx 10^{-3}\,\mathrm{J/m} \ll E_P$.

However, higher quench speeds v lead to higher fragment numbers (Fig. 3 *A* and *B*), reflecting the fact that the minimum fragment length λ decays with v (Fig. 3*D*). We can rationalize this using dimensional analysis. The dynamics of the rod are overdamped (Movies S4 and S5), so during a quench the force on any element scales as $F \sim v$. In 1D, force has units of energy density so we will balance F against the other fundamental energy density of the system, the potential energy density. The energy density of the kth bending mode scales as $E_k \sim k^4$, yielding $k \sim v^{1/4}$ and hence $\lambda \sim v^{-1/4}$ in agreement with the data (Fig. 3*D*). The same scaling is implied by the following more detailed argument. Assume the rod is approximately flat at time $t = 0$. The maximum strain in the overdamped rod at time t scales (*SI Appendix*, *Euler–Bernoulli Equation*) as $\epsilon^2_{\max} \sim r^2\kappa^2_{\max} \sim (vtr^2/L^3)$. However, as the rod is pushed, low-energy bending waves must necessarily equilibrate its shape. We balance the dominant frequency ω of these waves with the strain rate above, $\dot{\epsilon}^2_{\max} \sim (vr^2/tL^3) \sim \omega^2$. Finally, the dispersion relation for bending waves, $\omega \sim crk^2$ yields $v/tL^3 \sim c^2k^4$. This sets the wavenumber k in the equilibration wave packet for a given quench speed v. Our data indicate that λ is independent of the rod radius r (*SI Appendix*, Fig. S3), which suggests a role for acoustic waves triggered by the equilibration wavepacket. These acoustic waves will weaken the rod at their antinodal high-strain sites. At early times, the dominant acoustic wavenumber can be expected to match the dominant triggering bending wavenumber, yielding for the minimum fragment length $\lambda \sim k^{-1} \sim v^{-1/4}$. In 1D fragmentation the number of fractures sites N_f and the minimal fragment length λ are predicted (36) to scale as $\lambda \sim N_f^{-1}$. Combining these scaling results, we obtain the prediction $N_f \sim v^{1/4}$ at small v, in agreement with our data (Fig. 3*E*). In particular, this also explains why rods can undergo binary fracture when the quench velocity is very small (Fig. 3*A*). At sufficiently high quench speeds, the number of fracture sites, and hence the number of fragments, saturates (Fig. 3*E*). This can be understood in terms of stochastic fracture theory (*SI Appendix*, *Stochastic Fracture Theory*). The picture of quenched fragmentation which emerges is as follows: The quench speed releases bending and acoustic waves of particular wavelengths which weaken the rod in certain patterns. At low speeds the number of fracture sites simply increases as a power law, whereas at high speeds this growth is limited by the rate of subcritical crack growth.

Conclusions

We have demonstrated two distinct protocols for achieving controlled binary fracture in brittle elastic rods. By generalizing classical fracture arguments (12) to account for twisting and

quenching, we were able to rationalize the experimentally observed fragmentation patterns. Due to their generic nature, the above theoretical considerations can be expected to apply to torsional and kinetic fracture processes in a wide range of engineered (1) and natural (21, 22) 1D structures. Our experimental results suggest several directions for future research. New theory beyond the Kirchhoff model is needed to clarify conclusively the microscopic origin of the minimum fragment length. Moreover, a detailed experimental analysis of the crack propagation dynamics will require going beyond megahertz time resolution (Fig. 1). An interesting practical question is whether, and how, twist can be used to control the fracture behavior of 2D and 3D materials.

Materials and Methods

A comprehensive description of all experimental procedures and details of derivations is provided in *SI Appendix*.

Experiments. Rods were Barilla no. 1, 3, or 5 raw spaghetti of length $L = 24$ cm or 20 cm. Cameras used were Edgertronic SC2 (1,972 fps), Photron FASTCAM Mini AX200 (9,000 fps), and Phantom v611 (75,000 fps). Crack propagation was filmed with Phantom v611 at 10^6 fps, using a thicker spaghetti ($2r = 1.7$ mm) for improved visualization.

Simulations. The Kirchhoff equations were simulated with a discrete differential geometry algorithm (38, 39), using a Verlet time-stepping scheme. Each rod was discretized into 50 elements. One simulation time step corresponded to 1 μs of real time. Fracture was simulated by disconnecting the rod in one time step wherever the fracture criterion was satisfied.

ACKNOWLEDGMENTS. We thank Dr. Jim Bales [Massachusetts Institute of Technology (MIT)] and the MIT Edgerton Center for providing the high-speed cameras. This work was supported by an Alfred P. Sloan Research Fellowship (to J.D.) and a Complex Systems Scholar Award from the James S. McDonnell Foundation (to J.D.).

1. Hetényi M (1946) *Beams on Elastic Foundation: Theory with Applications in the Fields of Civil and Mechanical Engineering* (Univ Michigan Press, Ann Arbor, MI).
2. Gardiner B, Berry P, Moulia B (2016) Review: Wind impacts on plant growth, mechanics and damage. *Plant Sci* 245:94–118.
3. Virot E, Ponomarenko A, Dehandschoewercker É, Quéré D, Clanet C (2016) Critical wind speed at which trees break. *Phys Rev E* 93:023001.
4. Albrecht A, et al. (2016) Comment on "critical wind speed at which trees break". *Phys Rev E* 94:067001.
5. Peterlik H, Roschger P, Klaushofer K, Fratzl P (2006) From brittle to ductile fracture of bone. *Nat Mater* 5:52–55.
6. Hu DL, Chan B, Bush JWM (2003) The hydrodynamics of water strider locomotion. *Nature* 424:663–666.
7. Kantsler V, Goldstein RE (2012) Fluctuations, dynamics, and the stretch-coil transition of single actin filaments in extensional flows. *Phys Rev Lett* 108:038103.
8. Sanchez T, Chen DTN, DeCamp SJ, Heymann M, Dogic Z (2012) Spontaneous motion in hierarchically assembled active matter. *Nature* 491:431–434.
9. Broedersz CP, MacKintosh FC (2014) Modeling semiflexible polymer networks. *Rev Mod Phys* 86:995–1036.
10. Baughman RH, Zakhidov AA, de Heer WA (2002) Carbon nanotubes–The route toward applications. *Science* 297:787–792.
11. Bouchaud E (1997) Scaling properties of cracks. *J Phys Condens Matter* 9:4319–4344.
12. Audoly B, Neukirch S (2005) Fragmentation of rods by cascading cracks: Why spaghetti does not break in half. *Phys Rev Lett* 95:095505.
13. Gladden JR, Handzy NZ, Belmonte A, Villermaux E (2005) Dynamic buckling and fragmentation in brittle rods. *Phys Rev Lett* 94:035503.
14. Herrmann HJ, Hansen A, Roux S (1989) Fracture of disordered, elastic lattices in two dimensions. *Phys Rev B* 39:637–648.
15. Peerlings RHJ, de Borst R, Brekelmans WAM, Geers MGD (1998) Gradient-enhanced damage modelling of concrete fracture. *Mech Cohes-Frict Mat* 3:323–342.
16. Gerstle W, Sau N, Silling S (2007) Peridynamic modeling of concrete structures. *Nucl Eng Des* 237:1250–1258.
17. Evans E (2001) Probing the relation between force—lifetime—and chemistry in single molecular bonds. *Annu Rev Biophys Biomol Struct* 30:105–128.
18. Neuman KC, Nagy A (2008) Single-molecule force spectroscopy: Optical tweezers, magnetic tweezers and atomic force microscopy. *Nat Methods* 5:491–505.
19. Gilbert CJ, Ritchie RO, Johnson WL (1997) Fracture toughness and fatigue-crack propagation in a Zr–Ti–Ni–Cu–Be bulk metallic glass. *Appl Phys Lett* 71:476–478.
20. Demetriou MD, et al. (2011) A damage-tolerant glass. *Nat Mater* 10:123–128.
21. Tang-Schomer MD, Patel AR, Baas PW, Smith DH (2010) Mechanical breaking of microtubules in axons during dynamic stretch injury underlies delayed elasticity, microtubule disassembly, and axon degeneration. *FASEB J* 24:1401–1410.
22. Odde DJ, Ma L, Briggs AH, DeMarco A, Kirschner MW (1999) Microtubule bending and breaking in living fibroblast cells. *J Cell Sci* 112:3283–3288.
23. Attmannspacher U, Scharf BE, Harshey RM (2008) FliL is essential for swarming: Motor rotation in absence of FliL fractures the flagellar rod in swarmer cells of Salmonella enterica. *Mol Microbiol* 68:328–341.
24. Yu MF, et al. (2000) Strength and breaking mechanism of multiwalled carbon nanotubes under tensile load. *Science* 287:637–640.
25. Mokashi VV, Qian D, Liu Y (2007) A study on the tensile response and fracture in carbon nanotube-based composites using molecular mechanics. *Compos Sci Technol* 67:530–540.
26. Mott N (1947) Fragmentation of shell cases. *Proc R Soc Lond A Math Phys Sci* 189:300–308.
27. Wittel F, Kun F, Herrmann HJ, Kröplin BH (2004) Fragmentation of shells. *Phys Rev Lett* 93:035504.
28. Zhang H, Ravi-Chandar K (2006) On the dynamics of necking and fragmentation–I. Real-time and post-mortem observations in Al 6061-O. *Int J Fract* 142:183–217.
29. Mitchell NP, Koning V, Vitelli V, Irvine WTM (2017) Fracture in sheets draped on curved surfaces. *Nat Mater* 16:89–93.
30. Villermaux E (2017) Self-activated fragmentation. *Int J Fract* 206:171–193.
31. Sykes C (1996) *No Ordinary Genius* (Norton and Company Ltd., New York), pp 180–181.
32. Olympic Channel (2012) Lazaro Borges (CUB) snaps pole - Pole vault - London 2012 Olympics [video recording]. Available at https://www.youtube.com/watch?v=VrHiK1aHWL0. Accessed February 1, 2018.
33. Audoly B, Pomeau Y (2010) *Elasticity and Geometry* (Oxford Univ Press, Oxford), pp 59–104.
34. Coleman BD, Dill EH, Lembo M, Lu Z, Tobias I (1993) On the dynamics of rods in the theory of Kirchhoff and Clebsch. *Arch Ration Mech Anal* 121:339–359.
35. Graff KF (1975) Wave motion in elastic solids. (Dover, New York).
36. Grady DE (2010) Length scales and size distributions in dynamic fragmentation. *Int J Fract* 163:85–99.
37. Villermaux E (2007) Fragmentation. *Annu Rev Fluid Mech* 39:419–446.
38. Bergou M, Wardetzky M, Robinson S, Audoly B, Grinspun E (2008) Discrete elastic rods. *ACM Trans Graph* 27:63:1–63:12.
39. Bergou M, Audoly B, Vouga E, Wardetzky M, Grinspun E (2010) Discrete viscous threads. *ACM Trans Graph* 29:116:1–116:10.
40. Gerbode SJ, Puzey JR, McCormick AG, Mahadevan L (2012) How the cucumber tendril coils and overwinds. *Science* 337:1087–1091.
41. Goriely A (2006) Twisted elastic rings and the rediscoveries of Michell's instability. *J Elast* 84:281–299.
42. Panaitescu A, Grason GM, Kudrolli A (2018) Persistence of perfect packing in twisted bundles of elastic filaments. *Phys Rev Lett* 120:248002.
43. Kudrolli A, Chopin J (2018) Tension-dependent transverse buckles and wrinkles in twisted elastic sheets. *Proc R Soc A* 474:20180062.
44. McCormick AG (2013) Discrete differential geometry and physics of elastic curves. PhD thesis (Harvard University, Cambridge, MA).
45. Brutzer H, Luzzietti N, Klaue D, Seidel R (2010) Energetics at the DNA supercoiling transition. *Biophys J* 98:1267–1276.
46. Turcotte DL (1986) Fractals and fragmentation. *J Geophys Res Solid Earth* 91:1921–1926.
47. Danku Z, Kun F (2016) Fracture process of a fiber bundle with strong disorder. *J Stat Mech Theory Exp* 2016:073211.